AGU100 ADVANCING EARTH AND SPACE SCIENCE

JGR

Journal of Geophysical Research: Solid Earth

RESEARCH ARTICLE
10.1002/2017JB015098

Key Points:
- Dense arrays of seismometers can be calibrated from field data to obtain relative sensor orientations and gains to high precision
- Array calibration improves the computation of horizontal seismic strains that can be used with techniques of wave gradiometry
- Seismic array strain agrees well with observed strain from a borehole strain meter located at Pinyon Flat, California

Correspondence to:
C. A. Langston,
clangstn@memphis.edu

Citation:
Langston, C. A. (2018). Calibrating dense spatial arrays for amplitude statics and orientation errors. *Journal of Geophysical Research: Solid Earth*, *123*, 3849–3870. https://doi.org/10.1002/2017JB015098

Received 10 OCT 2017
Accepted 22 MAR 2018
Accepted article online 25 MAR 2018
Published online 8 MAY 2018

Calibrating Dense Spatial Arrays for Amplitude Statics and Orientation Errors

Charles A. Langston[1]

[1]Center for Earthquake Research and Information, University of Memphis, Memphis, TN, USA

Abstract An iterative procedure is designed to calibrate dense arrays of three-component seismic instruments for station amplitude statics and horizontal component orientation errors. Station amplitude statics refers to differences in sensor and digitizer gains and amplification effects due to local site and installation conditions. Amplitude statics and orientation errors can seriously affect computation of the wavefield gradient tensor that is the basis of seismic strain and rotation computations as well as analysis of wave field attributes through wave gradiometry since wave spatial gradients rely on first-order differences of the wavefield between sensors in an array. The technique is based on the assumption of a common wave field observed over a small array using teleseismic earthquake observations. In situ calibration of the broad band, 800-m aperture array at Pinyon Flat, California, achieves relative amplitude precision for vertical components of the array from 0.16% to 0.25% and horizontal components from 0.16% to 0.61%. Relative sensor orientations can be determined to a precision better than 0.35°. Comparison of horizontal strains computed from array observations of a regional M4.9 earthquake and strains from the Gladwin Tensor borehole strain meter at Pinyon Flat shows excellent correspondence over the frequency band of 0.05 to 2 Hz. Agreement of borehole measured strains and seismic array strains for regional/local seismic events gives confidence that a borehole strain meter and single, three-component, colocated seismometer can be used as a "point array" for deducing wavefield attributes from wave gradiometry.

Plain Language Summary Small changes in the wave strength over an array of many seismometers can quantify the distortion of the Earth as strain. In order to have an accurate estimate of strain each seismometer of the array must record the motions of the ground with high fidelity, to less than 1% error, and also must be oriented precisely relative to north. A mathematical method is developed in this study to precisely calibrate an array of 14 seismometers at the Pinyon Flat Observatory maintained by the University of California, San Diego, in order to compute accurate strains. Ground strain from a M4.9 earthquake in Southern California inferred from the array of calibrated seismometers was successfully compared to strain observed on a borehole strain meter in the center of the array. Results show that seismometers can be calibrated to a higher precision than given by manufacturer's specifications. The agreement between strains observed by the array of seismometers and the strain meter shows that the strain meter is also adequately calibrated and that, in principle, the strain meter can replace the array of seismometers for determining the direction and speed of seismic waves.

1. Introduction

The precision of seismic amplitude measurements is critical for estimating seismic wave spatial gradients used for inferring seismic strains, stresses, and rotations. First- and second-order spatial derivatives of the wavefield are finding use in new array techniques for inferring wave attributes such as propagation azimuth and horizontal phase velocity (e.g., de Ridder & Curtis, 2017; Langston & Liang, 2008; Liang & Langston, 2009; Liu & Holt, 2015). The purpose of this paper is to present a method for calibrating dense, three-component arrays of seismometers, often referred to as "geodetic" seismic arrays (Spudich et al., 1995), for vertical and horizontal component amplitude factors and relative horizontal component orientations.

Recorded seismic wave amplitudes will depend on the instrument transfer function, orientation of the instrument, physical characteristics of installation, and structure of the Earth under the site. In the best of situations, seismic instruments can be carefully calibrated in the laboratory before deployment. But the simple act of moving them from the lab to the field can change their characteristics, and each installation, at a minimum, will introduce errors in relative orientations. These problems, along with unavoidable human errors, can

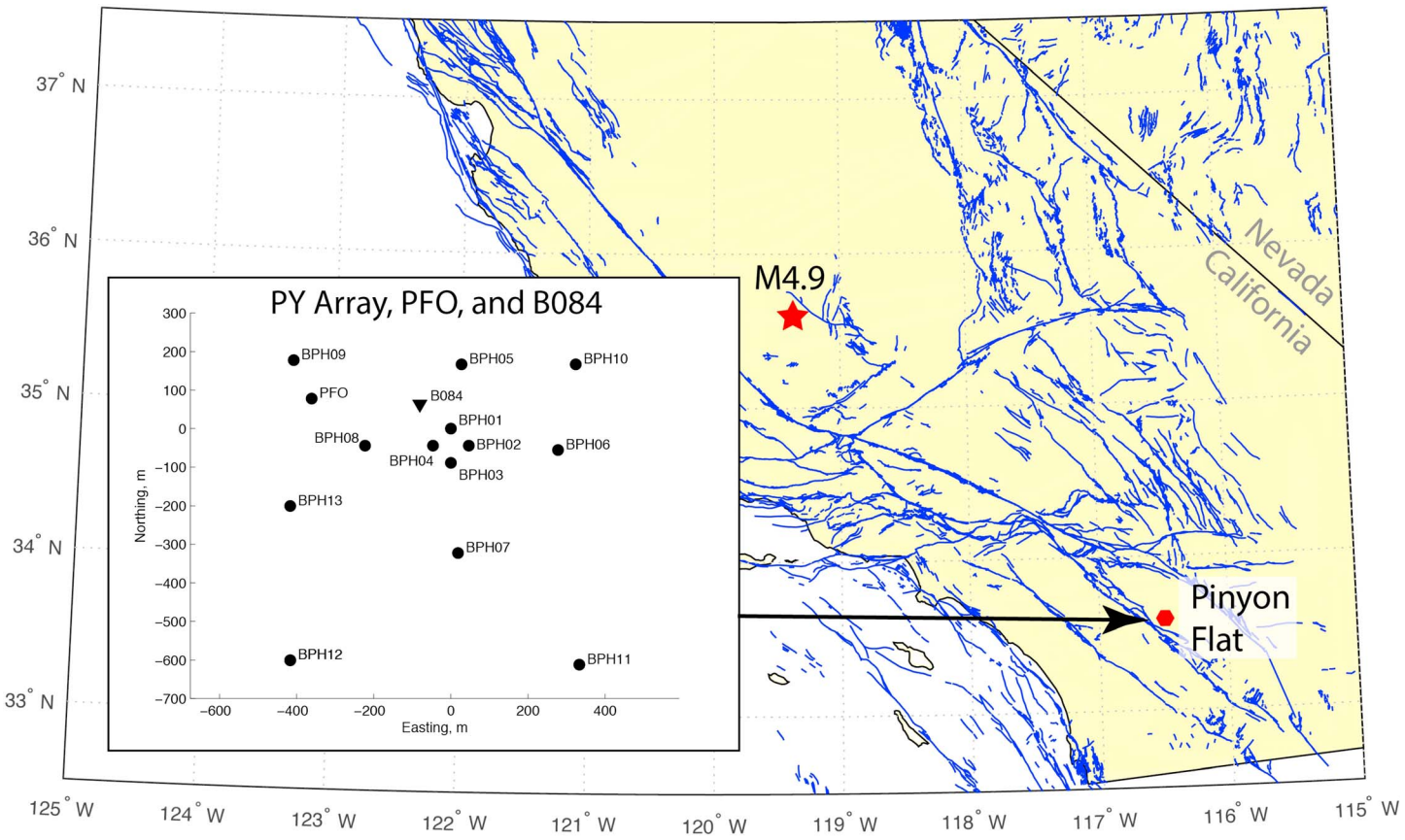

Figure 1. Map showing the location of the Pinyon Flat Observatory, a M4.9 earthquake examined in the text, and active faults of California and Nevada. The inset shows the geometry of the Pinyon Flat broadband array and the PBO B084 borehole strainmeter.

introduce significant variations in amplitude that degrade spatial gradient estimates of the wave field (Davis et al., 2005; Ekström et al., 2006; Hutt & Ringler, 2011).

A primary motivation for this work is to compute array-derived horizontal strains from the seismic array and compare them with those recorded by the Plate Boundary Observatory (PBO) Gladwin Tensor Strain Meter (GTSM) at Pinyon Flat, California, station B084. An experimental broadband array was installed within the area of the facility by the University of California, San Diego, starting in July 2014 and has been recording until the present. The original purpose of the array was to test installation procedures for two different broadband instruments, the Streckheisen STS-5 and Nanometrics T120 systems. Strains in the frequency band of 0.5 to 5 Hz can be estimated from the array and compared to strains observed by the GTSM within the array from local and regional earthquakes (Figure 1). Calibration of the strain instrument has been performed by Grant (2010) and Hodgkinson et al. (2013), so it is of considerable interest to see if array-derived strains are consistent with the GTSM strains. A recent study of teleseismic strain recorded by the laser strain meter at Pinyon Flat shows very good correspondence to seismic array-derived strains from the same teleseisms (Donner et al., 2017). The aperture of the array is only 800 m which limits its ability for long-period spatial gradient computations, but it is ideal for relatively high frequency local and regional earthquakes.

This paper is also the initial step in the logic of using a GTSM and a three-component seismic instrument as a "point array" (Langston & Liang, 2008) where the combination of horizontal strains and original horizontal displacement wavefield can be used with wave gradiometry (Langston, 2007b; Langston & Liang, 2008) to infer wave attributes of the *P-SV* wave components of the wavefield. Attributes include wave propagation azimuth, apparent velocity, geometrical spreading, and radiation pattern all computed at a single geographical point without using a spatially distributed seismic array. In order to arrive at this new seismic instrument or point array, several things need to be shown. The first is that existing calibration of the PBO GTSMs give accurate estimates of dynamic horizontal strains from the wavefield of local and regional earthquakes. This can be

done by comparing seismic array strains to GTSM strains. However, in order to compute accurate seismic array strains, confidence in the observed amplitudes must be developed through calibrating the Pinyon Flat array for amplitude statics and finding the relative orientations of all array elements. Demonstration of the similarity of array and GTSM strains at one installation can then be used to justify calibration of other PBO GTSM/seismic instruments as point arrays.

The goal of this paper is to present a method that is effective in calibrating static amplitude factors and relative instrument orientations of a dense seismic array to minimize errors in spatial gradient computations. The method will be applied to the Pinyon Flat broadband experiment to judge the stability and precision of seismic amplitudes and instrument orientations with time. We will be using an extensive database of 43 teleseismic earthquakes recorded at the array to examine the precision in array calibration. Detailed examination of array and GTSM strains will be touched on but will be more thoroughly presented in an additional paper.

2. Problems in the Computation of Array Spatial Gradients

The problems in estimating spatial gradients from seismic observations can be summarized by examining the central difference operator for a spatial derivative in one dimension of space and with time:

$$\frac{\partial u(t,x)}{\partial x}\Delta x+\frac{\partial u(t,x)}{\partial t}\Delta t\cong\frac{1}{2}\left\{u_i(t+\Delta t,x+\Delta x)-u_j(t-\Delta t,x-\Delta x)\right\} \tag{1.1}$$

where u_i and u_j are observations from two different seismometers, i and j, in a regularly spaced array. The time and space derivatives can be related to each other using a plane wave propagation model where

$$u(t,x)=af\left(t-\frac{x}{v}\right) \tag{1.2}$$

so that

$$\frac{\partial u}{\partial t}=-v\frac{\partial u}{\partial x} \tag{1.3}$$

to give

$$\frac{\partial u}{\partial x}=\frac{u_i(t+\Delta t,x+\Delta x)-u_j(t-\Delta t,x-\Delta x)}{2(\Delta x-v\Delta t)} \tag{1.4}$$

This central difference operator is accurate to second order in space and in time if x and t are exactly known independent variables. However, errors in determining the position and errors in time synchronization will introduce an additional error in using equation (1.4) to compute a spatial derivative.

Fortunately, errors due to timing and position are becoming negligible with modern instrumentation and field techniques. Differential GPS measurements can routinely determine relative seismometer positions to 1 cm for localized arrays with a nearby geodetic base station (Trimble, 2017). Assuming equation (1.4) with $\Delta t = 0$, the error, ε_x, in the spatial derivative due to error in positioning a site, δx, can be estimated by using the binomial theorem on the denominator giving

$$\frac{1}{\Delta x\pm\delta x}=\frac{1}{\Delta x}\left(\frac{1}{1\pm\frac{\delta x}{\Delta x}}\right)\simeq\frac{1}{\Delta x}\left(1\mp\frac{\delta x}{\Delta x}\right)=\frac{1}{\Delta x}(1\mp\varepsilon_x). \tag{1.5}$$

So with sites separated by only 10 m, a positioning error of 1 cm translates into an error in the spatial derivative of 10^{-3} or only 0.1%. This error decreases with increasing site separation.

Seismic timing systems guarantee relative timing of data samples at accuracies of the order of 1 to 10 μ s. For example, the commonly used Quanterra Q330HR system has an accuracy of 1 microsecond at a sampling rate of 100 Hz (Kromer, 2006a) and the Reftek RT130HR system has an accuracy of 5 microsecond at 100 Hz sampling (Kromer, 2006b). Normally, seismometers in an array are synchronized to a common time standard, such as GPS time, so that individual time data sampled across the array are considered to be simultaneous. If there is an error, say Δt, in recording for a plane wave propagating across the array, then the error due to time sampling will be equivalent to an error in spatial sampling given by $\delta x = v\delta t$ in the denominator of equation (1.5). For an error of 1 microsecond, a conservative high velocity of 10 km/s and spatial separation of 10 m the error in computing the spatial derivative due to system timing inaccuracy will also be of the order of 10^{-3} or 0.1%.

Like the error in positioning, the effect of the error in timing decreases as the separation distance increases between seismometers. It also decreases with the decreasing apparent velocity of the wave. Although these errors decrease as station separation increases, error in the Taylor's series approximation inherent in equation (1.4) increases as the square of separation distance. Timing errors are assumed to be negligible in the data analysis performed in this paper based on Kromer's studies. We manipulate waveforms point by point and do not incorporate time shifts that might occur if the maximum of the correlation of two traces is taken.

By far, the most serious problem with computing numerical spatial derivatives concerns the fidelity of recorded amplitudes. As relation (1.4) shows, the spatial derivative is proportional to amplitude differences between sensors. In the absence of errors in sensor positions and timing, equation (1.4) reduces to

$$\frac{\partial u}{\partial x} = \frac{u_i(t, x + \Delta x) - u_j(t, x - \Delta x)}{2\Delta x} \tag{1.6}$$

If each sensor has a static multiplicative amplitude factor due to calibration differences, recorder gains, or local site conditions such that

$$u_i = A_i u(t, x) \tag{1.7}$$

and

$$A_i = 1 + \varepsilon_i \tag{1.8}$$

then the computed spatial gradient will be

$$\left.\frac{\partial u}{\partial x}\right|_{\text{computed}} = \left.\frac{\partial u}{\partial x}\right|_{\text{true}} + \varepsilon_i \frac{u(t, x + \Delta x) - \frac{\varepsilon_j}{\varepsilon_i} u(t, x - \Delta x)}{2\Delta x} \tag{1.9}$$

where

$$\left.\frac{\partial u}{\partial x}\right|_{\text{true}} = \frac{u(t, x + \Delta x) - u(t, x - \Delta x)}{2\Delta x} \tag{1.10}$$

If the amplitude errors ε_i and ε_j are the same, then the computed gradient will just be 1 + ε_i times the true gradient. A mixture of different amplitude errors will create a computed gradient that will contain the actual gradient plus proportions of the original displacements. What this usually means is that the computed gradient will degrade as frequency decreases since the spatial gradient is proportional to the time gradient (i.e., particle velocity—equation (1.3)) and the Fourier spectrum of the time gradient is intrinsically higher frequency than the original wave field. This was pointed out by Langston (2007a) and was the subject of studies by Poppeliers and Evans (2015) and Barker and Langston (2016) to determine limitations on array dimensions in computing spatial gradients and use in wave gradiometry calculations.

Thus, the effect of timing and position errors in computing spatial gradients for modern arrays can be made quite small (~0.1% or less) by using high-quality equipment and careful geodetic siting. The stability of amplitude measurements, however, has continued to be a chronic problem in seismology. Instrument manufacturers often advertise that instrument response functions and gains are good to approximately 1% in amplitude and that ground motion component directions within the instrument have tolerances of less than 1°. However, broadband instruments may degrade due to environmental or mechanical problems (Davis et al., 2005; Ekström et al., 2006; Hutt & Ringler, 2011) and show substantial frequency-dependent and even nonlinear amplitude changes of 50% or more at periods greater than the low-frequency corner of the velocity response. Simple errors, such as incorrectly programming instrument gain, in fielding an array are always possible and may introduce additional puzzling amplitude behavior.

The orientation of three-component sensors in the field is dependent on the method of orienting the horizontal axis of the sensor with local true north, a process that is subject to several sources of error (Ringler et al., 2013). Misorientation of horizontal components can easily introduce apparent amplitude errors between sensors of several percent or more. Recent work over the past 10 years has shown that Global Seismic Network instrument orientations are usually better than ±5° but occasionally have significant errors of up to 20° (Ekstrom & Busby, 2008). Larger errors have been attributed to use of magnetic compasses to orient instruments (Aderhold et al., 2015; Ringler et al., 2013) rather than using more accurate methods, such as an optical gyroscope. Details of site installations such as using sealed or unsealed vaults versus burying the

seismometer in the ground may also introduce additional sources of noise and ground seismometer coupling or tilting that will affect recorded amplitudes (e.g., Aderhold et al., 2015). However, there are few studies that have examined the problem of how site conditions can affect absolute amplitudes at high precision since it is difficult to have the necessary control on the seismic wave source. In the related problem of relative amplitude, Barker and Langston (2016) showed that the relative amplitude response of standard exploration geophones changed by about 3% between various huddle tests made in soil; the effect was attributed to seismometer/soil coupling. Recognizing that many sources of error can affect seismic wave amplitude across an array of seismometers, we will develop an empirical method to detect and correct for amplitude differences and sensor orientations in situ.

3. Pinyon Flat Broadband Array

The broadband array at Pinyon Flat consists of 13 stations under the Incorporated Research Institutions in Seismology (IRIS) array code "PY" and the 14th consisting of the permanent station PFO in the seismic vault at Pinyon Flat (Figure 1). The PY array was installed 7–10 April 2014 by personnel of the University of California, San Diego, in 2–3-m shallow boreholes, but all sensors were pulled from each site and reinstalled 7–12 July 2014. At this time the array consisted of eight Nanometrics T120 and five STS-5 broadband posthole seismometers. After 13–15 November 2014, seismometers at nine sites were removed and replaced with different STS-5 or T120 instruments resulting in a total of six T120 and seven STS-5 instruments across the array. Because of the equipment change in the early history of the array, we will only be using teleseismic earthquake data recorded after 15 November 2014. Calibrating an array for orientation and amplitude statics requires data from stations that have not been moved or changed in any way after installation since, obviously, the simple act of reinstalling the instrument may introduce different errors in orientation.

4. Method

4.1. Array Calibration

The process of array calibration is an exercise in determining relative amplitudes of recorded ground motions among the various stations of the array since there is no instrument with absolutely known orientation or response characteristics. The nominal instrument responses were used to correct data to filtered ground displacement so that the STS-5s, T120s, and STS-2 data could be directly compared. However, the expectation was that each instrument may have small differences in sensitivity and that gain factors in the digitizers may also be different to give digital amplitude differences of a few percent. The calibration method will be based on the following assumptions, some of which can be checked after the analysis:

1. Instrument characteristics (sensitivity, gain, orientation) do not change with time.
2. Instruments are misoriented horizontally but not vertically and instrument horizontal components are orthogonal.
3. Each ground motion component has a different but constant amplitude multiplier.
4. Teleseismic signals recorded by all instruments are identical in phase and amplitude.

Assumption (1) will naturally be investigated by examining calibration as a function of time using teleseisms that have occurred from November 2014 to May 2016.

Assumption (2) is a restriction that arises from the behavior of the inverse problem for sensor orientation and relative amplitudes and will be discussed later.

Assumption (3) seems unduly restrictive in that instrument response functions could have errors that are a function of frequency. This initial attempt at array calibration will assume a constant amplitude multiplier but the method allows estimates to be obtained as a function of frequency by band-pass filtering.

Assumption (4) can be made strongest of them all by taking time windows of low-frequency teleseismic waves. The 14-station array has an aperture of 800 m. High signal-to-noise teleseismic data from events greater than M6.5 were used in the frequency band from 0.005 to 0.05 Hz (200 to 20 s period). A two-pole acausal Butterworth filter was used in filtering the data such that the dominant energy of the signal was in

the 50 to 20 s period band, generally above the long-period corner of the instrument responses. Surface waves dominated the waveforms for most of the events in the teleseismic catalog. Minimum horizontal wavelengths are approximately 60 km, 2 orders of magnitude greater than the array dimension guaranteeing that wave phase differences between array elements will be small. Body wave and surface wave phase time differences across the array will depend on wave type. The greatest time difference between the nearest and farthest station will only be 0.27 s for a 20-s Rayleigh wave traveling at a horizontal phase velocity of 3 km/s. Theoretically, for two identical instruments, this would reduce the zero lag correlation coefficient between the waves by about 0.03% which, as will be shown below, is an order of magnitude smaller than the variability in the data. A long time window of 60 min duration for vertical, north-south, and east-west data starting 1 min before the *P* wave arrival was incorporated in the inversion simply to use all of the available data and to make sure that horizontal components were composed of independent wave types.

Assumption (2) above allows the separation of the vertical component and horizontal component calibrations as two different inverse problems. Consider the vertical displacements of two different stations, $z_0(t)$ and $z_1(t)$, of the array from the same teleseism:

$$\begin{aligned} z_0(t) &= c_0 u_3(t) \\ z_1(t) &= c_1 u_3(t) \end{aligned} \tag{1.11}$$

where the different sensitivity and gains between instruments are reflected in different amplitude multipliers, c_0 and c_1, respectively. Since there is no way to know the input ground motion $u_3(t)$ independently, we can at least determine the amplitude of $z_1(t)$ relative to $z_0(t)$ by combining equations (1.11)

$$z_1(t) = \frac{c_1}{c_0} z_0(t) \tag{1.12}$$

The time dependence can be removed by making $z_0(t)$ the reference waveform and forming the inner product, or zero lag correlation,

$$\langle z_0(t), z_1(t) \rangle = \int_{-\infty}^{+\infty} z_0(t) z_1(t) \mathrm{d}t \tag{1.13}$$

with relation (1.12) to give

$$r_{z_{01}} = \frac{c_1}{c_0} = \frac{\langle z_0(t), z_1(t) \rangle}{\langle z_0(t), z_0(t) \rangle}. \tag{1.14}$$

This effectively uses all of the amplitude data within the chosen time window for estimating relative amplitudes since the inner product is an estimate of the cross power contained within the time interval of both signals. This also reduces the complexity of the inverse problem by reducing thousands of time series samples to one number.

The amplitude ratio, $r_{z_{ij}}$, of every vertical component z_j relative to z_i is

$$r_{z_{ij}} = \frac{c_j}{c_i} = \frac{\langle z_i(t), z_j(t) \rangle}{\langle z_i(t), z_i(t) \rangle} \tag{1.15}$$

This can be cast into a linear system of equations by taking the natural logarithm of the amplitude ratios

$$\ln r_{z_{ij}} = \ln c_j - \ln c_i \tag{1.16}$$

It is apparent that

$$\ln r_{z_{ij}} = -\ln r_{z_{ji}} \tag{1.17}$$

and

$$\ln r_{z_{ii}} = 0 \tag{1.18}$$

The $\ln c_i$ coefficients can be found using the same method that VanDecar and Crosson (1990) suggested for finding optimal average travel time residuals from body wave correlation measurements:

$$\mathbf{Gm} = \mathbf{d} \tag{1.19}$$

where

$$\mathbf{G} = \begin{bmatrix} -1 & 1 & 0 & 0 & \cdots & 0 \\ -1 & 0 & 1 & 0 & \cdots & 0 \\ -1 & 0 & 0 & 0 & \cdots & 1 \\ 0 & -1 & 1 & 0 & \cdots & 0 \\ \vdots & \vdots & \vdots & \vdots & \vdots & \vdots \\ 1 & 1 & 1 & 1 & \cdots & 1 \end{bmatrix} \tag{1.20}$$

$$\mathbf{m} = \begin{bmatrix} \ln c_1 \\ \ln c_2 \\ \vdots \\ \ln c_n \end{bmatrix} \tag{1.21}$$

$$\mathbf{d} = \begin{bmatrix} \ln r_{z_{12}} \\ \ln r_{z_{13}} \\ \vdots \\ \ln r_{z_{1n}} \\ \ln r_{z_{23}} \\ \vdots \\ 0 \end{bmatrix} \tag{1.22}$$

and where the equation of constraint

$$\sum_{i=1}^{n} \ln c_i = 0 \tag{1.23}$$

has been added to the last row of **G** to ensure that the relative amplitudes average to unity. This system is linear, has a unique solution, and yields relative amplitudes that can be used to correct vertical component data by dividing by the amplitude coefficient, c_i. In addition to being a linear problem, the solution uses the relative amplitudes of all sensor pairs to find the optimum array average. Although there is no guarantee that the resulting corrections will yield the actual ground motion at the array, if the sensor calibrations are unbiased, negative and positive amplitude perturbations should tend to cancel out yielding something close to the actual ground motion.

Simultaneous inversion for amplitude static coefficients and seismometer orientation using the horizontal components is more involved since the orientation and component amplitude statics are coupled. Starting with the coordinate system in Figure 2, observed "east-west" $e_i(t)$ and "north-south" $n_i(t)$ displacements for the ith station are given in terms of the common displacement in the geographical coordinate system (u_1,u_2) as

$$\begin{aligned} e_i(t) &= a_i[u_1(t)\cos\delta_i - u_2(t)\sin\delta_i] \\ n_i(t) &= b_i[u_1(t)\sin\delta_i + u_2(t)\cos\delta_i] \end{aligned} \tag{1.24}$$

where the a_i and b_i are unknown amplitude static coefficients for the observed east-west and north-south components of the ith station. Solving equation (1.24) for the ground displacements in the true geographical coordinate system gives

$$\begin{aligned} u_1(t) &= \alpha_i e_i(t)\cos\delta_i + \beta_i n_i(t)\sin\delta_i \\ u_2(t) &= -\alpha_i e_i(t)\sin\delta_i + \beta_i n_i(t)\cos\delta_i \end{aligned} \tag{1.25}$$

where

$$\alpha_i = a_i^{-1} \text{ and } \beta_i = b_i^{-1} \tag{1.26}$$

Note that no summation is implied by repeated indices in any of the equations of this paper. Since (u_1, u_2) are the same for all instruments, the horizontal components of the jth instrument can be compared to the ith instrument by substituting equation (1.25) into equation (1.24) for the jth instrument. After some manipulation of trigonometric identities this gives

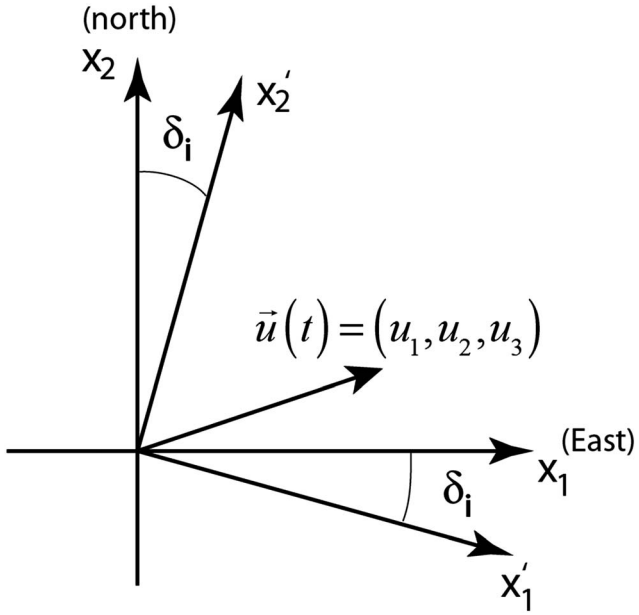

Figure 2. Coordinate system for developing the inverse problem for horizontal component statics and orientation. The unprimed system is the geographic coordinate system. Each seismometer *i* may be misoriented by an amount δ_i. Horizontal ground motion is resolved into the coordinate system of each seismometer.

$$\begin{aligned} e_j(t) &= a_j\alpha_i e_i(t)\cos\delta_{ij} - a_j\beta_i n_i(t)\sin\delta_i \\ n_j(t) &= b_j\alpha_i e_i(t)\sin\delta_{ij} + b_j\beta_i n_i(t)\cos\delta_i \end{aligned} \tag{1.27}$$

and where

$$\delta_{ij} = \delta_j - \delta_i \tag{1.28}$$

is the difference in azimuths between stations. Forming inner products of the components of the *i*th station with the *j*th

$$\begin{aligned} A_{ij} &= \langle e_i(t), e_j(t)\rangle \\ B_{ij} &= \langle n_i(t), n_j(t)\rangle \\ C_{ij} &= \langle e_i(t), n_j(t)\rangle \\ D_{ij} &= \langle n_i(t), e_j(t)\rangle \end{aligned} \tag{1.29}$$

and applying these to equations (1.27) gives a system of coupled equations

$$\begin{aligned} A_{ij} &= a_j\alpha_i A_{ii}\cos\delta_{ij} - a_j\beta_i C_{ii}\sin\delta_{ij} \\ B_{ij} &= b_j\alpha_i C_{ii}\sin\delta_{ij} + b_j\beta_i B_{ii}\cos\delta_{ij} \\ C_{ij} &= b_j\alpha_i A_{ii}\sin\delta_{ij} + b_j\beta_i C_{ii}\cos\delta_{ij} \\ D_{ij} &= a_j\alpha_i C_{ii}\cos\delta_{ij} - a_j\beta_i B_{ii}\sin\delta_{ij} \end{aligned} \tag{1.30}$$

Better insight can be obtained if only two stations are considered, say station 1 (a reference station) and station *j*. In this case

$$\begin{aligned} A_{1j} &= a_j\alpha_1 A_{11}\cos\delta_{1j} - a_j\beta_1 C_{11}\sin\delta_{1j} \\ B_{1j} &= b_j\alpha_1 C_{11}\sin\delta_{1j} + b_j\beta_1 B_{11}\cos\delta_{1j} \\ C_{1j} &= b_j\alpha_1 A_{11}\sin\delta_{1j} + b_j\beta_1 C_{11}\cos\delta_{1j} \\ D_{1j} &= a_j\alpha_1 C_{11}\cos\delta_{1j} - a_j\beta_1 B_{11}\sin\delta_{1j} \end{aligned} \tag{1.31}$$

There are four equations but five (coupled) unknowns: α_1, a_j, β_1, b_j, and δ_{1j}. If one or more of the unknowns are fixed, then there is a chance that these equations could be solved for the other unknowns. Tasič and Runovc (2013) show that if the generator constants (and digitizer gains) are known for one instrument, inversion of the Euler matrix for a second instrument with unknown orientation recording the same signal can give the generator constants (and gains) for a second instrument along with the relative orientation of the second with respect to the first. Here the assumption is that the generator constants and gains are not known for any component for any instrument. Nevertheless, the solution of equations (1.31) requires that at least one quantity be known. That quantity is chosen to be the east-west component of one particular station where α_1 is set to 1 and the orientation relative to north, δ_{11}, is zero. The inversion problem is then reduced to finding a_j, β_1, b_j, and δ_{1j} with this constraint. The problem is expanded to all stations where the solution of β_1 can be found by simultaneously using the waveform data for all stations rather than station by station which this system of equations could allow.

It is straightforward to pose this system of equations as a standard, iterative least squares problem. Simplifying equations (1.31) by using a reference station (i = 1) gives the final set of equations for j = 2, … n stations of the array:

$$\begin{aligned} A_{1j} &= f_j = a_j A_{11}\cos\delta_{1j} - a_j\beta_1 C_{11}\sin\delta_{1j} \\ B_{1j} &= g_j = b_j C_{11}\sin\delta_{1j} + b_j\beta_1 B_{11}\cos\delta_{1j} \\ C_{1j} &= h_j = b_j A_{11}\sin\delta_{1j} + b_j\beta_1 C_{11}\cos\delta_{1j} \\ D_{1j} &= k_j = a_j C_{11}\cos\delta_{1j} - a_j\beta_1 B_{11}\sin\delta_{1j} \end{aligned} \tag{1.32}$$

Each function f_j, g_j, h_j, and k_j is expanded in a Taylor's series to linearized the problem, for example,

$$f_j(\mathbf{m}_j) \cong f_j(\mathbf{m}_{j0}) + \Delta\mathbf{m}_j^T \nabla f_j(\mathbf{m}_{j0}) \tag{1.33}$$

$\mathbf{m}_j = (\beta_1, a_j, b_j, \delta_{1j})^T$ is the model vector for each station j and $\mathbf{m}_{j0}$ the starting model or model from the previous iteration. Analytic derivatives for the gradient function are determined from simple differentiation of

equations (1.32) and are given in Appendix A. Equations (1.32) and (1.33) are collected up for all stations of the array except for the reference station to build the system of equations

$$\mathbf{G}\Delta\mathbf{m} = \Delta\mathbf{d} \tag{1.34}$$

where

$$\mathbf{G} = \begin{bmatrix} \frac{\partial f_2}{\partial \beta_1} & \frac{\partial f_2}{\partial a_2} & \frac{\partial f_2}{\partial b_2} & \frac{\partial f_2}{\partial \delta_{12}} & 0 & 0 & 0 & 0 & \cdots & 0 \\ \vdots & \vdots & \vdots & \vdots & 0 & 0 & 0 & 0 & \cdots & 0 \\ \frac{\partial k_2}{\partial \beta_1} & \frac{\partial k_2}{\partial a_2} & \frac{\partial k_2}{\partial b_2} & \frac{\partial k_2}{\partial \delta_{12}} & 0 & 0 & 0 & 0 & \cdots & 0 \\ \frac{\partial f_3}{\partial \beta_1} & 0 & 0 & 0 & \frac{\partial f_3}{\partial a_3} & \frac{\partial f_3}{\partial b_3} & \frac{\partial f_3}{\partial \delta_{13}} & 0 & \cdots & 0 \\ \vdots & \vdots & \vdots & \vdots & \vdots & \vdots & \vdots & 0 & \cdots & 0 \\ \frac{\partial k_3}{\partial \beta_1} & 0 & 0 & 0 & \frac{\partial k_3}{\partial a_3} & \frac{\partial k_3}{\partial b_3} & \frac{\partial k_3}{\partial \delta_{13}} & 0 & \cdots & 0 \\ & & & & \text{and so on} & & & & & \end{bmatrix}, \tag{1.35}$$

$$\Delta\mathbf{m} = \begin{bmatrix} \beta_1 - \beta_1^0 \\ a_2 - a_2^0 \\ b_2 - b_2^0 \\ \delta_{12} - \delta_{12}^0 \\ \vdots \\ a_n - a_n^0 \\ b_n - b_n^0 \\ \delta_{1n} - \delta_{1n}^0 \end{bmatrix}, \tag{1.36}$$

and

$$\Delta\mathbf{d} = \begin{bmatrix} A_{12} - f_1(\mathbf{m}_{1_0}) \\ B_{12} - g_1(\mathbf{m}_{1_0}) \\ C_{12} - h_1(\mathbf{m}_{1_0}) \\ D_{12} - k_1(\mathbf{m}_{1_0}) \\ \vdots \\ A_{1n} - f_n(\mathbf{m}_{n_0}) \\ B_{1n} - g_n(\mathbf{m}_{n_0}) \\ C_{1n} - h_n(\mathbf{m}_{n_0}) \\ D_{1n} - k_n(\mathbf{m}_{n_0}) \end{bmatrix} \tag{1.37}$$

It should be understood that the partial derivatives in the **G** matrix are evaluated at the starting model or previous iteration model.

For well-calibrated instruments in an array, a sensible starting model is to assume that all orientation corrections are zero and all amplitude coefficients equal to unity (1). Perversely, assuming that all orientations are perfect causes decoupling between the a_j, b_j, and β_1 coefficients of equations (1.32) which produces a **G** matrix less than full rank. In particular, there is complete trade-off between β_1 and b_j. To overcome this and relying on the fact that real array element deployments will not have perfect orientations, we use the empirical expedient that the first two iterations of the inversion do not include β_1. At that point, relative orientations can be resolved and β_1 is included as an inversion parameter. The inversion generally converged to the final parameter values within four iterations (Figure 3) and was not starting model dependent. In fact, synthetic tests showed that the inversion always converged even with very large perturbations to orientations of 45°. It is conceivable that inversion of other array data sets containing greater noise or unstable instrument characteristics would need different stabilization methods. It is likely that inversion for β_1 would have to be dropped since it was seen to be associated with the smallest singular value in the inversion. In this case, both horizontal components of the reference station become independent and the standard reference components for the horizontal components of all other stations.

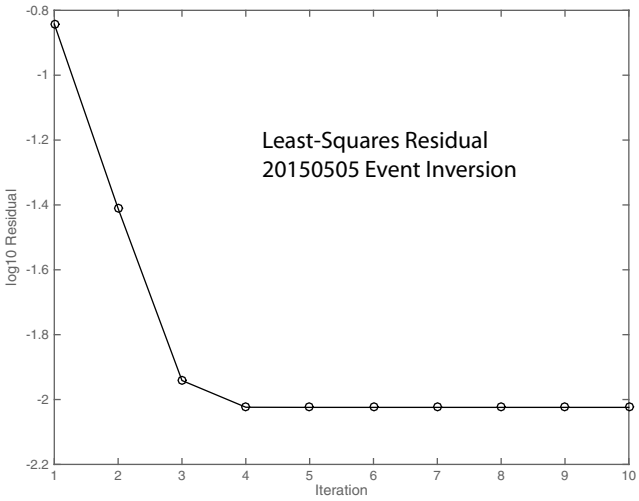

Figure 3. Typical behavior of the least squares residual with iteration for the horizontal component statics and orientation problem. The log (base 10) of the residual before inversion in each iteration is plotted versus iteration number. The inversion quickly converges after four iterations with this data set. The residuals show an order of magnitude improvement in fit of relative amplitudes between the *NS* and *EW* components of all stations of the array. Inversion is for the 5 May 2015 event (Table 1).

The vertical component inversion is identical to that proposed by VanDecar and Crosson (1990) in their study of relative travel time residuals. It has a desirable property that corrections are determined relative to an average over the array. One may think that the average value will be more representative of the actual ground motion than choosing one particular station as a reference, as done in the horizontal components inversion. An attempt was made to apply the idea behind VanDecar and Crosson (1990) by finding all relative *EW* and *NS* amplitudes along with all relative station orientations by using each station as a reference station. The relative amplitudes and orientations could then be inverted individually using Van Decar and Crosson's method to find optimum values. Unfortunately, this does not work because the amplitude factors and orientations are coupled through equations (1.30).

Nevertheless, there is a simple method that can be used to jointly normalize all *EW* and *NS* amplitude factors after inversion that preserves the exact coupling between amplitude and orientation, particularly preserving *EW* and *NS* amplitude ratios. Considering only one seismometer, suppose an inversion yields the relative amplitude factors, a and b. One way to remove bias in the sum of horizontal component amplitude is simply to average the horizontal amplitude factors and find the amplitude multiplier that sets the average to unity

$$d_0\left[\frac{a+b}{2}\right]=1 \tag{1.38}$$

such that a/b found from inversion is preserved. This can be expanded to include all horizontal station factors determined from the array through the relation

$$\frac{1}{2n}d_0\sum_{i=1}^{n}(a_i+b_i)=1 \tag{1.39}$$

giving the common factor

$$d_0=\frac{2n}{\sum_{i=1}^{n}(a_i+b_i)} \tag{1.40}$$

The product of d_0 and each a_i and b_i is then taken to get the adjusted amplitude static coefficients. The inverse of these new amplitude statics coefficients are the amplitude correction factors that are multiplied with the displacement component waveforms. This adjustment works because the inversion method is insensitive to the absolute value of the reference component. This method was used in the horizontal amplitude inversions that follow.

4.2. Computation of Array Spatial Gradients

Wavefield spatial gradients and the wavefield at the location of the B084 borehole strainmeter (Figure 1) were computed from the array data using a small innovation of the Taylor series method used by many previous authors (e.g., Langston, 2007a; Langston & Liang, 2008; Poppeliers & Evans, 2015; Spudich et al., 1995). The spatial gradients are considered to be nonuniform and terms of up to second order are kept in the Taylor's expansion for displacement:

$$u(x_i,y_i)\cong u(x_0,y_0)+\left.\frac{\partial u}{\partial x}\right|_0(x_i-x_0)+\left.\frac{\partial u}{\partial y}\right|_0(y_i-y_0)+\left.\frac{1}{2}\frac{\partial^2 u}{\partial x^2}\right|_0(x_i-x_0)^2+\left.\frac{1}{2}\frac{\partial^2 u}{\partial y^2}\right|_0(y_i-y_0)^2 +\left.\frac{\partial^2 u}{\partial x\partial y}\right|_0(x_i-x_0)(y_i-y_0) \tag{1.41}$$

The seismic observations at the location of array elements (x_i, y_i) are the data, and the desired quantities are $u(x_0, y_0)$ and the first derivatives. (x_0, y_0) will be the location of the borehole strainmeter.

Inversion for these quantities is straightforward. The system of equations is of the form

$$\mathbf{Gm} = \mathbf{d} \tag{1.42}$$

with the least squares solution being

$$\mathbf{m} = \left(\mathbf{G}^{\mathbf{T}}\mathbf{G}\right)^{-1}\mathbf{G}^{\mathbf{T}}\mathbf{d} \tag{1.43}$$

where

$$\mathbf{G} = \begin{bmatrix} 1 & (x_1 - x_0) & (y_1 - y_0) & \frac{1}{2}(x_1 - x_0)^2 & \frac{1}{2}(y_1 - y_0)^2 & (x_1 - x_0)(y_1 - y_0) \\ \vdots & \vdots & \vdots & \vdots & \vdots & \vdots \\ 1 & (x_n - x_0) & (y_n - y_0) & \frac{1}{2}(x_n - x_0)^2 & \frac{1}{2}(y_n - y_0)^2 & (x_n - x_0)(y_n - y_0) \end{bmatrix} \tag{1.44}$$

$$\mathbf{m} = \begin{bmatrix} u(x_0, y_0) \\ \left.\frac{\partial u}{\partial x}\right|_0 \\ \left.\frac{\partial u}{\partial y}\right|_0 \\ \left.\frac{\partial^2 u}{\partial x^2}\right|_0 \\ \left.\frac{\partial^2 u}{\partial y^2}\right|_0 \\ \left.\frac{\partial^2 u}{\partial x \partial y}\right|_0 \end{bmatrix} \tag{1.45}$$

and

$$\mathbf{d} = \begin{bmatrix} u(x_1, y_1) \\ \vdots \\ u(x_n, y_n) \end{bmatrix} \tag{1.46}$$

The advantage of this method, if the data support it, is that the wavefield can be interpolated to any point within or outside of the array and that a reference station is not needed. The resulting wavefield at the desired reference point now becomes a weighted average of all of the data in the array rather than relying on a difference (i.e., $u(x_i, y_i) - u(x_0, y_0)$) that will bias the derivatives depending on the amplitude statics behavior of the reference station displacement component. The least squares solution (1.43) is linear and well behaved since there are 6 unknowns for 14 independent equations. Incorporating the second derivatives is also a significant improvement since a propagating seismic wave does not create a uniform strain or rotation field as it propagates. By definition, the resulting inferred wavefield is accurate to third order in station separation.

4.3. Pinyon Flat Array Calibration

A data set of 43 high-quality teleseisms (Table 1) was compiled from over 50 events of M6.8 or larger recorded by the Pinyon Flat array from July 2014 to May 2016. Parameters came from the United States Geological Survey National Earthquake Information Center's Preliminary Determination of Epicenters bulletin. Event backazimuths reflect locations along the subduction zones of the Pacific Ocean (Figure 4). Some events were discarded because of obvious local transients occurring at one or more stations of the array. Events before 15 November 2014 were also not considered after an initial attempt at determining relative amplitude statics factors and orientations. It was realized that biases in amplitude factors and orientations before and after 15 November 2016 were a reflection of the array deployment history. In addition, an error in the instrument response metadata was also discovered (and corrected at the IRIS datacenter during this work) that was related to equipment changes for stations BPH01 and BPH02 in November 2014. At a minimum, it was interesting to note that applying the calibration technique seemed to be an effective quality control process that illuminated changes that had occurred over the history of the array.

In all cases, vertical and horizontal component inversions improved the relative amplitude behavior of three-component filtered displacements across the array (Figure 5). Being linear with no model or data null spaces, each vertical component inversion was perfectly resolved. Horizontal component inversions converged

Table 1
Teleseismic Event Parameters

Date/time	Latitude (deg)	Longitude (deg)	Depth (km)	M_W
2016-05-28/T09:46:59.780Z	−56.2409	−26.9353	78	7.2
2016-05-28/T05:38:50.540Z	−21.9731	−178.1987	405.58	6.9
2016-05-18/T16:46:43.860Z	0.4947	−79.616	29.95	6.9
2016-04-28/T19:33:24.070Z	−16.0429	167.3786	24	7
2016-04-16/T23:58:36.980Z	0.3819	−79.9218	20.59	7.8
2016-04-15/T16:25:06.220Z	32.7906	130.7543	10	7
2016-04-13/T13:55:17.800Z	23.0944	94.8654	136	6.9
2016-04-03/T08:23:52.320Z	−14.3235	166.8551	26	6.9
2016-03-02/T12:49:48.110Z	−4.9521	94.3299	24	7.8
2016-01-30/T03:25:12.220Z	53.9776	158.5463	177	7.2
2016-01-24/T10:30:30.230Z	59.6363	−153.4051	129	7.1
2015-12-09/T10:21:48.530Z	−4.1064	129.5079	21	6.9
2015-12-07/T07:50:05.950Z	38.2107	72.7797	22	7.2
2015-12-04/T22:25:00.110Z	−47.6165	85.0913	35	7.1
2015-11-24/T22:50:54.370Z	−10.0598	−71.0184	620.56	7.6
2015-11-24/T22:45:38.880Z	−10.5372	−70.9437	606.21	7.6
2015-11-18/T18:31:04.570Z	−8.8994	158.4217	12.59	6.8
2015-11-11/T02:46:19.830Z	−29.5097	−72.0585	10	6.9
2015-11-11/T01:54:38.570Z	−29.5067	−72.0068	12	6.9
2015–11-07/T07:31:43.870Z	−30.8796	−71.4519	46	6.8
2015-10-26/T09:09:42.560Z	36.5244	70.3676	231	7.5
2015-10-20/T21:52:02.560Z	−14.8595	167.3028	135	7.1
2015-09-16/T23:18:41.850Z	−31.5622	−71.4262	28.41	7
2015-09-16/T22:54:32.860Z	−31.5729	−71.6744	22.44	8.3
2015-07-27/T21:41:21.710Z	−2.6286	138.5277	48	7
2015-07-27/T04:49:46.400Z	52.376	−169.4458	29	6.9
2015-06-17/T12:51:32.790Z	−35.3639	−17.1605	10	7
2015-05-30/T11:23:02.110Z	27.8386	140.4931	664	7.8
2015-05-22/T23:59:33.770Z	−11.1093	163.2154	10	6.8
2015-05-22/T21:45:19.480Z	−11.0559	163.6959	11.19	6.9
2015-05-20/T22:48:53.420Z	−10.8759	164.1694	11	6.8
2015-05-12/T21:12:58.890Z	38.9056	142.0317	35	6.8
2015-05-12/T07:05:19.730Z	27.8087	86.0655	15	7.3
2015-05-07/T07:10:19.590Z	−7.2175	154.5567	10	7.1
2015-05-05/T01:44:06.380Z	−5.4624	151.8751	55	7.5
2015-05-01/T08:06:03.480Z	−5.2005	151.7773	44	6.8
2015-04-25/T06:11:25.950Z	28.2305	84.7314	8.22	7.8
2015-03-29/T23:48:31.010Z	−4.7294	152.5623	41	7.5
2015-02-13/T18:59:12.230Z	52.6487	−31.9016	16.68	7.1
2015-01-23/T03:47:27.050Z	−17.0309	168.52	219.96	6.8
2014-11-26/T14:33:43.640Z	1.9604	126.5751	39	6.8
2014-11-15/T02:31:41.720Z	1.8929	126.5217	45	7.1

Note. Date format is in yyyy-mm-dd.

uniformly within four to five iterations (e.g., Figure 3). Normalized correlation coefficients for vertical components even before inversion were quite high and greater than 0.999. Correlation coefficients for horizontal component waveforms were slightly smaller but generally larger than 0.98. After inversion horizontal component correlations were greater than 0.995. Changes in horizontal waveforms could be visually discerned after inversion (Figure 5).

It is difficult to assess the errors in the resulting amplitude correction factors for any one teleseismic event inversion. There is always improvement, and the data for each event are effectively noise free as seen by the high correlation coefficients before and after inversion. An estimate of the error can be made by taking the ensemble of all event inversions over the two and a half year time period (Figures 6–8). The amplitude factor inversions show remarkable stability and precision over this time period and are independent of the reference station taken for horizontal component inversions. In these plots, the amplitude correction factor is the number that is multiplied with the waveform data to correct it to produce uniform wave amplitude across the array. A low correction factor means that the observed ground motion component

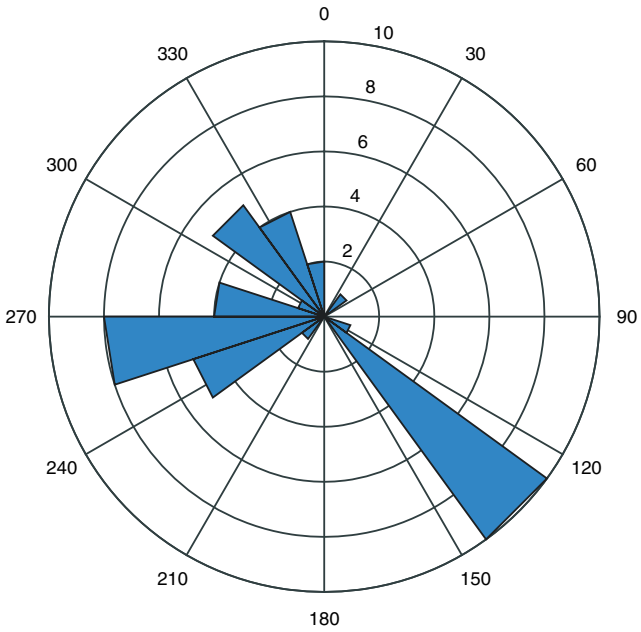

Figure 4. Histogram of back azimuth for the teleseismic earthquakes used for array calibration.

was higher amplitude. Vertical component amplitude correction factors between stations vary by only 1% and have a precision (one standard deviation) of 0.25% (Figures 6 and 7, Table 2). Horizontal components show greater variation in precision of up to 0.61%, but amplitude corrections are usually within 1%.

It is interesting to examine a histogram of station residuals of the natural log amplitude correction factors for all events (Figure 7). The vertical component residuals appear to follow a bimodal distribution between −0.01 and 0.01 consisting of slightly lower (negative) STS-5/STS-2 amplitude residuals compared to higher T120 residuals. The three distinct instrument types can be easily seen in the horizontal residuals histograms from three separate peaks.

By far, the most stable determination is horizontal orientation (Figure 8, Table 2). Orientation is as precise as 0.35° (one standard deviation) to as little as 0.05°. These relative orientations agree quite closely with those determined by Donner et al. (2017) who used a correlation grid search method, but no corrections for amplitude statics.

5. Discussion

The most striking result of this study is that the inferred relative amplitudes between the seismological outputs of vertical, *EW*, and *NS* components of these three seismometer types are quite consistent with one another and within the expectation of 1% differences in their respective generator constants. This is all the more remarkable since all three seismometers are constructed in the homogeneous triaxial geometry (Wielandt, 2002) where ground motion output is the combination of three mutually orthogonal sensor axes 54.7° from the vertical:

$$\begin{bmatrix} E \\ N \\ Z \end{bmatrix} = \frac{1}{\sqrt{6}} \begin{bmatrix} -2 & 1 & 1 \\ 0 & \sqrt{3} & \sqrt{3} \\ \sqrt{2} & \sqrt{2} & \sqrt{2} \end{bmatrix} \begin{bmatrix} U \\ V \\ W \end{bmatrix} \tag{1.47}$$

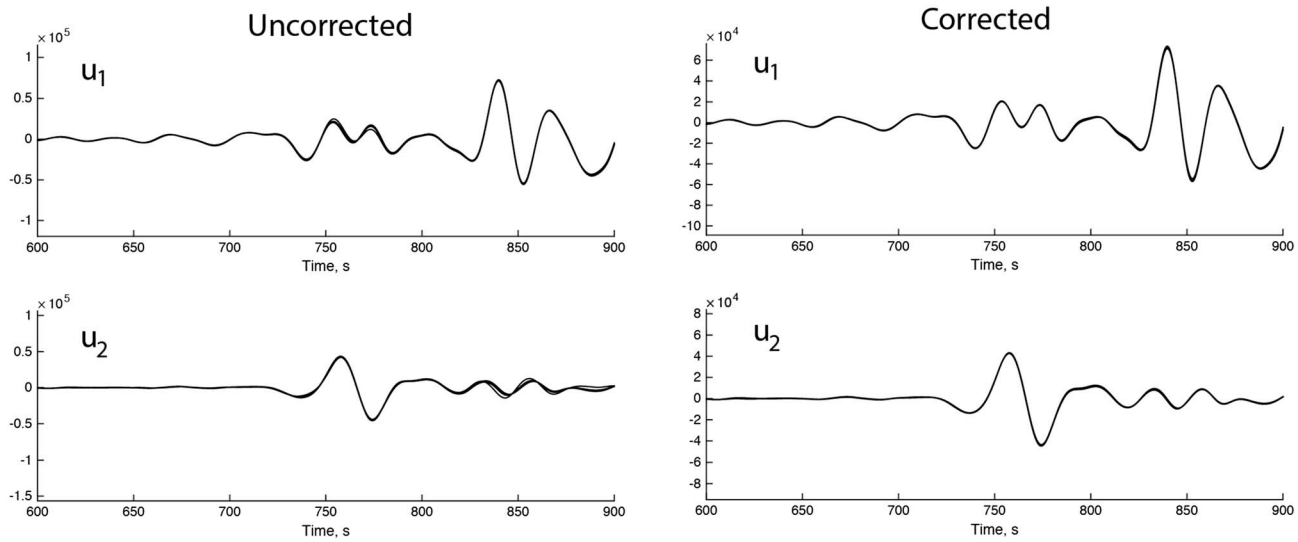

Figure 5. An example of uncorrected (left column) and corrected (right column) waveforms for the broadband array. Three hundred seconds of *EW* (u_1) and *NS* (u_2) waveforms from the 5 May 2015 event are shown for the 14 stations of the array. The uncorrected waveforms show very good correlation. Even so, horizontal waveforms corrected for amplitude statics and relative orientation overlay each other.

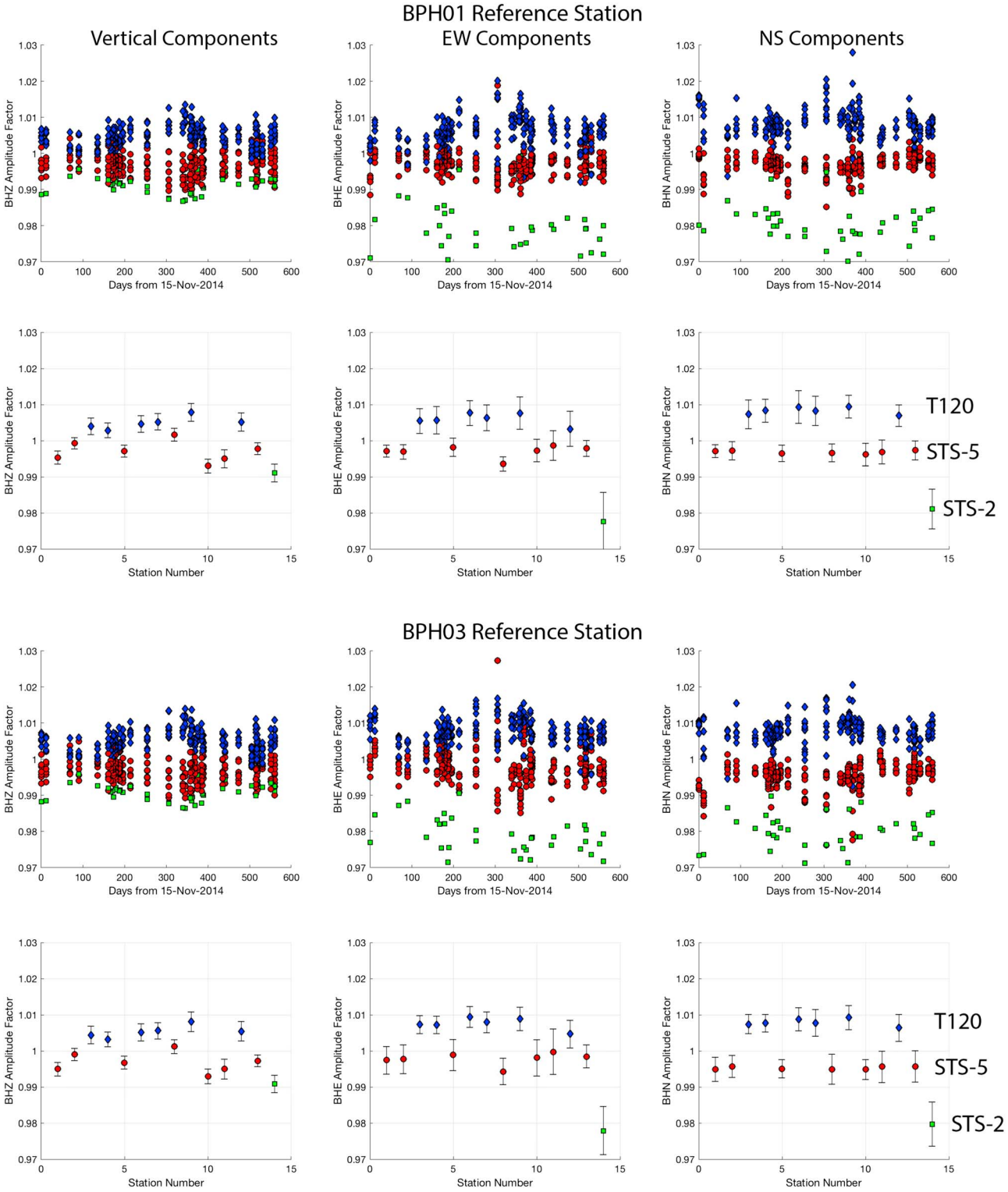

Figure 6. Plots of amplitude corrections for the vertical (left column), *EW* (middle column), and *NS* (right column) components of the array relative to station BPH01 (first and second rows) and BPH03 (third and fourth rows). The top plots for each station show amplitude correction factors as a function of Julian day from 15 November 2014 for all stations. The lower set of plots per assumed reference station show the mean amplitude correction factor with one standard deviation computed from all teleseism inversions. Station number is in the order of BPH01 (station 1) and so on. Station PFO is station 14. The horizontal components are seen to group into clusters of like instruments. T120, STS-5, and STS-2 instruments are denoted by blue diamonds, red circles, and green squares, respectively. There may be a hint of seasonal variation particularly for the vertical component amplitude factors. The STS-2 variation has a peak-to-peak annual variation of about 0.01. T120 and STS-5 factors seem to anticorrelate with greater dispersion in the results during late fall and early winter.

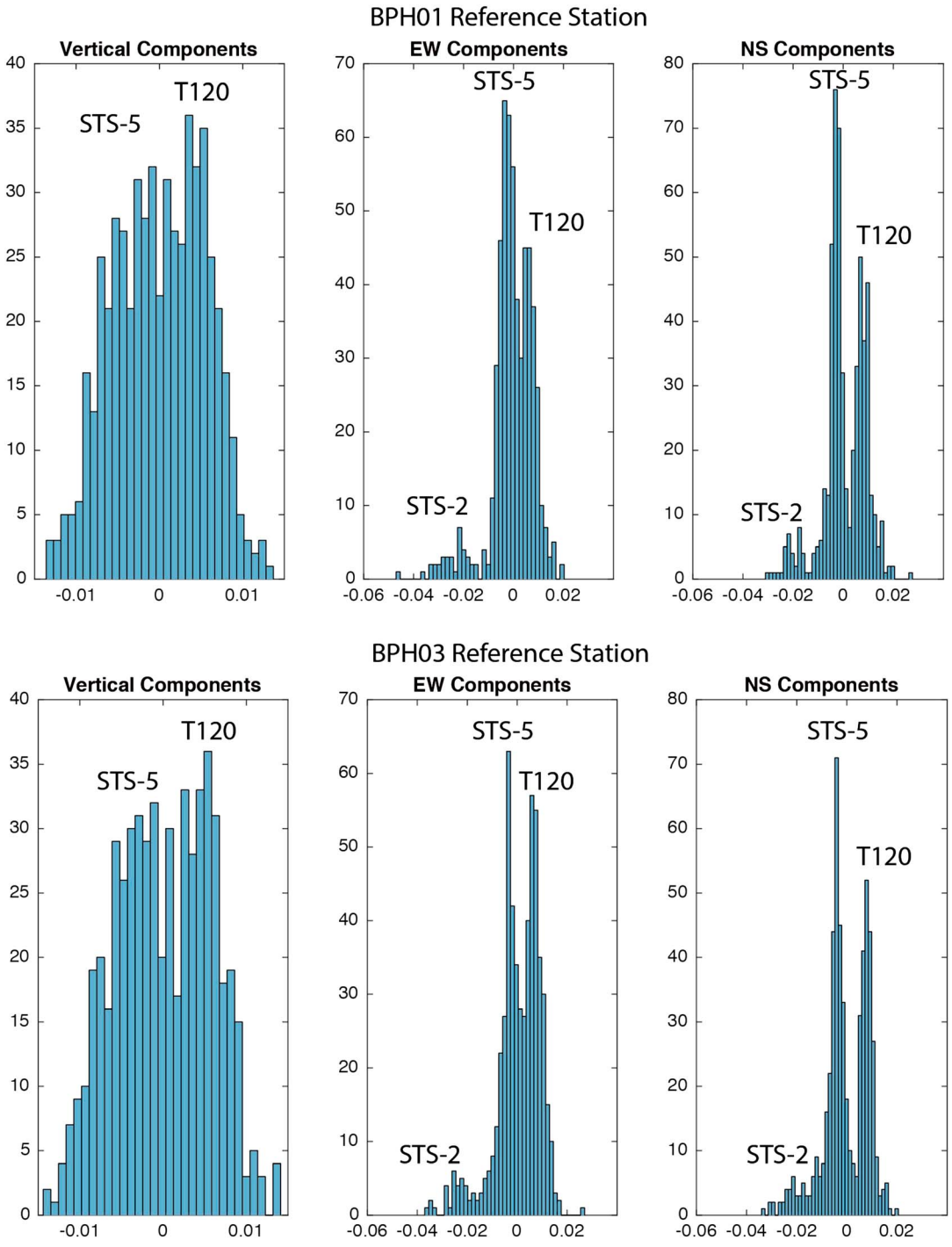

Figure 7. Histograms of the deviation of individual natural log station amplitude correction factors for all 43 teleseismic inversions shown for vertical (left column), *EW* (middle column), and *NS* (right column) components. The top set is from assuming BPH01 as the reference station and the bottom set from assuming BPH03 as the reference station. The horizontal components show distinct groupings that correlate with instrument type: STS-2 (PFO station), STS-5, and T120.

From the amplitude correction factors shown in Figures 6 and 7, it appears that output from STS-5 seismometers for the vertical components are biased slightly higher than nominal by about 0.5% compared to the T120 system which are biased lower by 0.5%. The STS-2 sensor records amplitudes approximately 2% greater than the other sensor types perhaps reflecting differences between portable and observatory installations or intrinsic to the instrument itself. The *Z* components are the average of the *U*, *V*, and *W*

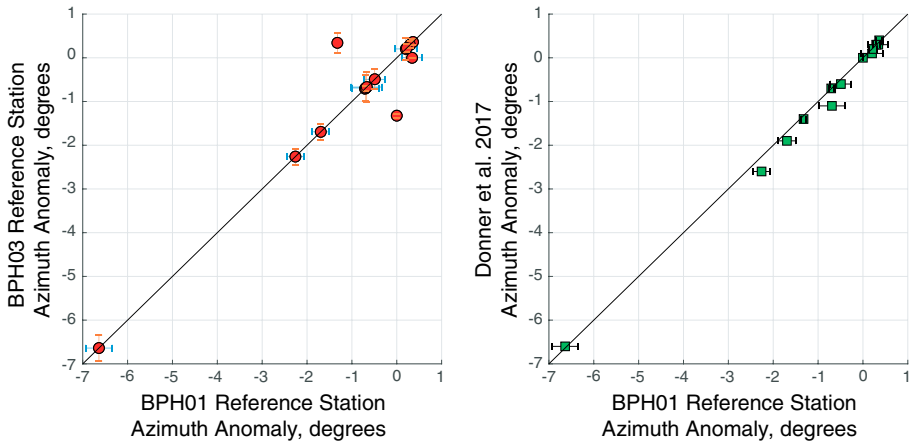

Figure 8. Correlation scatter plots for relative sensor orientations. The left panel shows the correlation between azimuth anomaly using BPH01 as the reference station (ordinate) versus using BPH03 as the reference station (abscissa). The right panel displays the correlation between the BPH01 results obtained here (ordinate) with those found by Donner et al. (2017) using a cross-correlation technique. See also Table 2.

components (equation (1.47)) that would tend to average differences in output between the internal sensors.

There appear to be larger and more distinct differences between sensor types for the *EW* and *NS* components, however (Figures 6 and 7). The differences in *EW* and *NS* component residuals for the T120 system compared to the STS-5 may be related to differences in output between *V* and *W* for the *NS* component compared to incorporating all three internal components for the *EW* component. The larger horizontal component errors may also be a result of small misalignments in the sensors related to the assumption of orthogonal *EW* and *NS* components (assumption 2 above).

Another logical possibility for explaining much of the instrument differences may be in how instrument transfer functions are determined by instrument and digitizer manufacturers. Afterall, the data that were used in the inversions required that theoretical instrument transfer functions be removed before analysis. Mathematically, the instrument differences determined here could be removed through corrections to the transfer functions. However, this might not be generally possible if station site conditions or installation practices affect gains.

Table 2
Amplitude Statics Correction Factors and Relative Orientations Assuming BPH01 as the Reference Station

Station	Z	σ_Z	EW	σ_{EW}	NS	σ_{NS}	δ (deg)	σ_δ (deg)	δ^a (deg)
BPH01	0.9953	0.0018	0.9971	0.0017	0.9971	0.0018	0	0	0
BPH02	0.9993	0.0016	0.9969	0.002	0.9972	0.0025	−1.32	0.05	−1.4
BPH03	1.004	0.0023	1.0055	0.0035	1.0073	0.0039	0.34	0.23	0.3
BPH04	1.0029	0.002	1.0057	0.0038	1.0084	0.0032	0.2	0.25	0.1
BPH05	0.9971	0.0017	0.9982	0.0025	0.9965	0.0023	−0.71	0.06	−0.7
BPH06	1.0046	0.0024	1.0077	0.0034	1.0093	0.0045	−0.49	0.23	−0.6
BPH07	1.0052	0.0023	1.0063	0.0036	1.0083	0.0041	−1.69	0.19	−1.9
BPH08	1.0016	0.0018	0.9936	0.0019	0.9965	0.0025	0.36	0.06	0.4
BPH09	1.0079	0.0025	1.0077	0.0045	1.0095	0.0031	−6.64	0.3	−6.6
BPH10	0.9931	0.0019	0.9972	0.0031	0.9962	0.0031	0.3	0.08	0.3
BPH11	0.9951	0.0025	0.9987	0.0041	0.9969	0.0033	−0.69	0.3	−1.1
BPH12	1.0052	0.0025	1.0033	0.0048	1.007	0.003	−2.26	0.18	−2.6
BPH13	0.9978	0.0016	0.9979	0.0022	0.9973	0.0027	0.22	0.1	0.2
PFO	0.9911	0.0024	0.9776	0.008	0.9811	0.0055	−0.67	0.35	N/A

Note. Also displayed are the relative station orientations from Donner et al. (2017). N/A = not applicable.
[a]Relative sensor orientations from Donner et al. (2017)

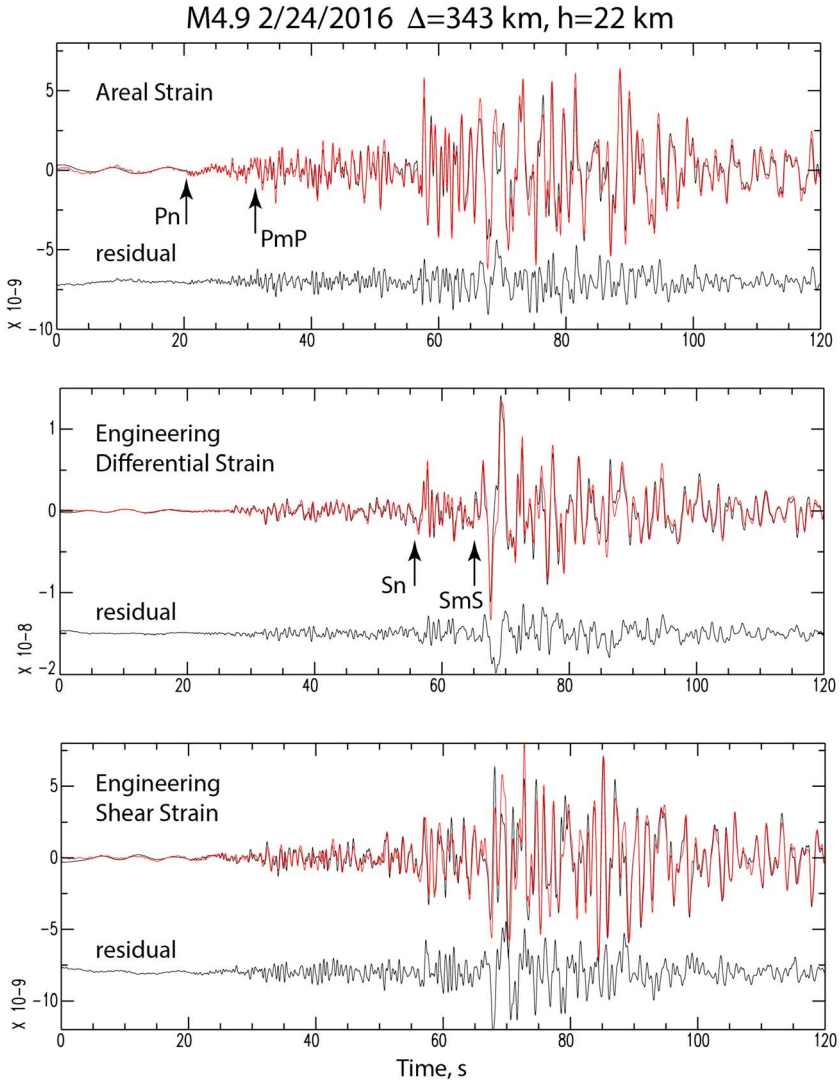

Figure 9. Comparison of broadband strains inferred from the B084 GTSM (red) and strains computed at the B084 location using the broadband seismic array (black). Data come from the M4.9 20160224 regional event (Figure 1). Residuals are calculated by differencing the seismograms and are displayed beneath waveform pairs. Also shown are major *P* and *S* wave arrivals in the seismograms. Waveform phases agree throughout but the residuals appear to be significant suggesting that the borehole GTSM response could be improved. A passband of 0.05 to 2 Hz is used.

Identifying u with the *EW* and v with *NS* components, horizontal displacement gradients were calculated using (1.43)–(1.46) which were then used to form the areal strain

$$\frac{\partial u}{\partial x}+\frac{\partial v}{\partial y} \tag{1.48}$$

engineering differential strain

$$\frac{\partial u}{\partial x}-\frac{\partial v}{\partial y} \tag{1.49}$$

engineering shear strain

$$\frac{\partial u}{\partial y}+\frac{\partial v}{\partial x} \tag{1.50}$$

and rotation about the vertical axis

$$\frac{\partial u}{\partial y} - \frac{\partial v}{\partial x} \tag{1.51}$$

for data from a M4.9 regional earthquake (Figure 1) recorded by the array and B084 GTSM borehole instrument (Figure 9). Calibration constants for the B084 strainmeter were taken from a study by Grant (2010) who compared strains computed from long-period teleseisms recorded by the ANZA broadband array to borehole instrument strains within the array.

Two considerations are required in comparing array strains with strain meter strains. The first is that the strain meter gauges are buried at a depth of approximately 160 m relative to the surface array. An appropriate comparison of seismic waves recorded by both facilities requires that seismic wavelengths be significantly longer than the strain meter depth so that the free surface effect cannot be seen in the data. A reasonable criterion is that seismic wavelengths be at least 4 times the strain meter depth. Assuming that high-frequency surface waves might have velocities as low as 1 km/s gives a high-frequency limit of about 2 Hz for comparing waves from local and regional earthquakes.

The aperture of the seismic array defines the second consideration in that the computation of accurate strains is limited by the quality of the instrument response and calibration. The results of the calibration suggest that strains should be accurate to better than 10% for wave lengths 100 times the array aperture (Langston, 2007b) or for waves of about 80 km in wavelength. A regional *P* wave with velocity of 6 km/s has an 80 km wavelength for 13 s period. A band pass between 0.05 and 2 Hz is chosen to compare array and GTSM strains.

The comparison between borehole and array strains for this regional event is remarkable (Figure 9) considering the relatively broad passband (0.05 to 2 Hz). This is the subject of a detailed follow-on study of array and borehole strains and strainmeter calibration issues. However, the good agreement suggests that previous borehole strainmeter calibration was very effective and that calibrated borehole strainmeters can provide an accurate representation of the wavefield from regional and local earthquakes. The strain wavefield from strain instruments can then be incorporated into wave gradiometry analyses to determine wave field attributes (e.g., Langston & Liang, 2008) to serve as a "point" array seismic instrument. Small differences seen in the strains of Figure 9 may have a source in biases of the seismic array calibration or biases in the GTSM calibration. Further work is needed to investigate both issues.

After all is said and done, has this array calibration method made a difference in computing spatial gradients? The answer is "yes" for three different reasons. In the initial phase of this study, array strains were computed using data that were corrected using the instrument metadata that came with the initial data download from the IRIS Data Management Center. After correcting for each instrument response, it appeared that two stations, BPH01 and BPH02, had 25% higher amplitudes than the others for early regional events. This made a significant difference in computing array strains. Applying the array calibration method using the teleseismic data immediately indicated that this was a real problem and that it was time dependent over the life of the array deployment. Further research on array deployment history uncovered the instrument changes that occurred and a simple error in not including the correct instrument response file in the metadata. So, amplitude calibration proved to be an effective quality control method.

Secondly, even with correct instrument metadata, further calibration of the array improved the computation of both displacements and strains of the wavefield (Figure 10). Finally, it is good to have knowledge of array quality for future use in strain meter calibration studies and gradient studies of the wavefield. Array calibration should be performed, if at all possible, for geodetic arrays before use in estimating wave spatial gradients.

There are several aspects of the calibration method that warrant comment. The first is obvious in that the method finds only relative amplitudes and orientations between ground motion components and station orientations. This improves the derivative calculation, but clearly, any bias in orienting an array, say all stations consistently misoriented by 10° or all gains off by a constant factor, will cause a bias in the spatial derivatives.

Implicit but important aspects of the inversion are the choice of frequency band to consider as well as the length of time window for the data seismograms. An array of broadband sensors recording large teleseisms allows a choice of frequency band that guarantees that wavelengths be several orders of magnitude larger than the array aperture. Most teleseismic earthquakes display their dominant energy in the 100-to-20 s

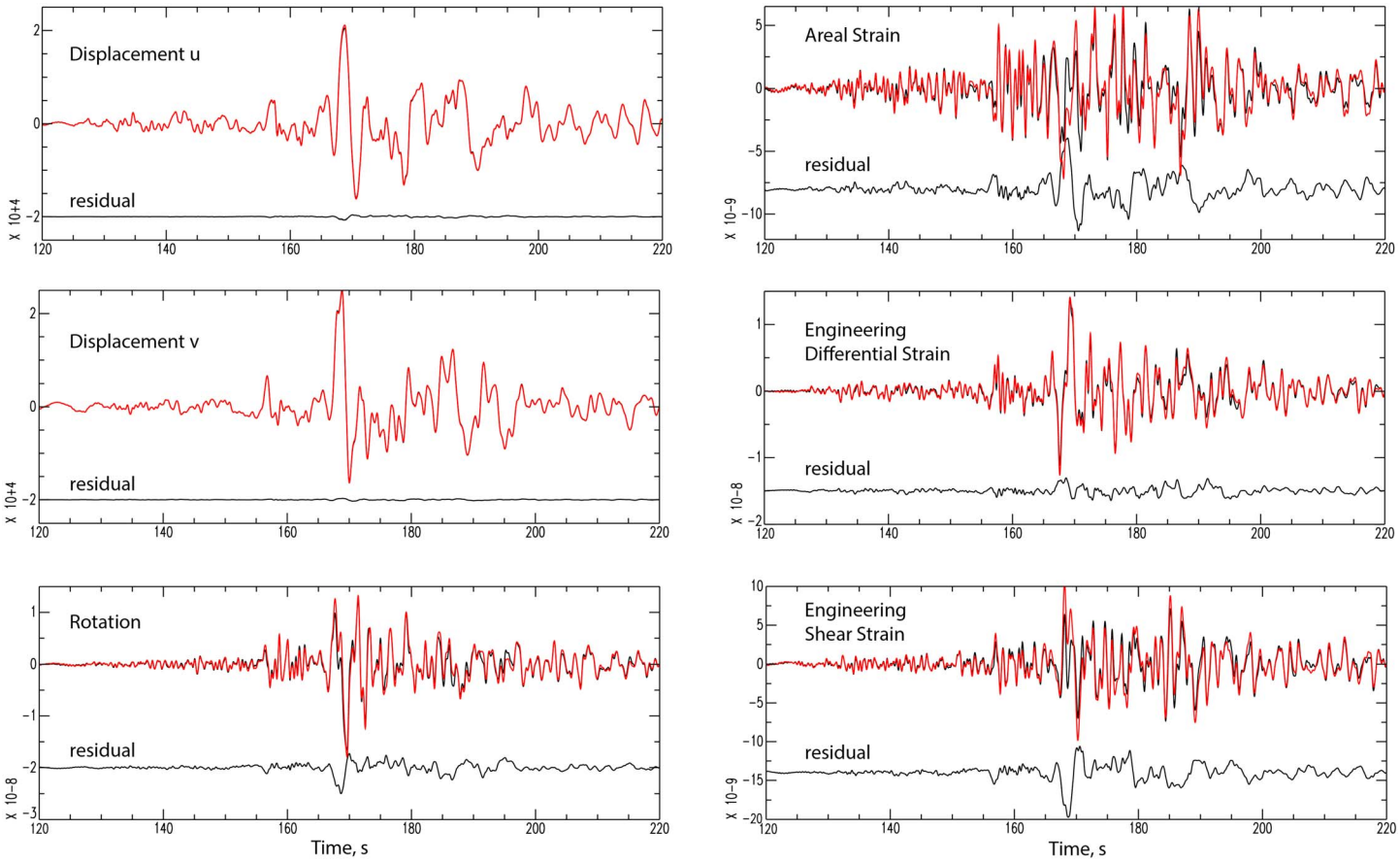

Figure 10. (left column) Comparison of corrected (black) and uncorrected (red) *EW* displacement (*u*), *NS* displacement *v*, and array vertical rotations, respectively, at the location of the borehole strain meter for the M4.9 regional event. The difference in seismograms is shown as a residual waveform below each pair. Residuals are small for the displacements but become significant for rotation about the vertical axis. Unit for displacement is nanometers. (right column) Comparison of areal, engineering differential, and engineering shear strains between corrected (black) and uncorrected (red) array data. Residuals are significant strongly suggesting that the array calibration improved computation of array strains and rotations. A passband of 0.05 to 2 Hz is used.

period band (0.01 to 0.05 Hz) for displacement because of long trains of surface waves. *P* waveforms are often much smaller, but *S* waveforms may also be relatively large and start off the surface wave trains. It is appropriate to choose a relatively long time window to encompass these waves so that artifacts created by band-pass filtering and time windowing do not enter the inversion.

Another odd characteristic of the inversion for horizontal amplitude factors and relative orientation is that the common displacements (u_1, u_2) in equation (1.24) should be independent such that u_1 is not proportional to u_2. If u_1 and u_2 are not independent, then the relative orientation trades off directly with amplitude factors; the inversion becomes nonunique. Having a mix of different wave types on the horizontal components, such as SH/SPL and/or Love/Rayleigh guarantees that the common displacements will be independent. Hence, time windows should be taken to incorporate these diverse wave types.

The effect on the amplitude inversion by choice of frequency band was investigated in a numerical experiment for one teleseism (28 May 2016, Table 1). Vertical and horizontal component inversions were run for data that were band-pass filtered in the bands of 0.005–0.05 Hz, 0.025–0.05 Hz, and 0.05–0.1 Hz. The first two frequency bands are appropriate for the size of the array in that expected errors due to wave propagation should be less than 0.03%. Inversion results for the two low-frequency bands differed by only 0.0–0.3% in vertical amplitude factor, 0.0–1.0% in horizontal amplitude factor, and less than 0.3° in relative orientation. These variations are within those observed using the ensemble of earthquakes (Figure 6). Variations between the low-frequency and high-frequency inversions followed the same behavior suggesting that choice of frequency band is not particularly important for broadband stations as long as the expected horizontal wavelengths are an order of magnitude greater than array aperture.

Finally, an attempt was made to cast the inverse problem with all three Euler angles (Bronshtein et al., 2004) in a way similar to the method suggested by Tasič and Runovc (2013), but the very small expected deviations from the vertical cause a significant trade-off between the azimuth and the nutation angle around the perturbed vertical direction. This could be minimized if the generator constants and orientations of all three components of a reference station are assumed to be perfectly known to reduce the severity of coupling between each axis. However, in the attempt to find all the relative amplitudes of horizontal components based just on one standard component at the reference station, it proved expedient to avoid this nonuniqueness in the inverse problem by decoupling vertical component inversion from horizontal component analysis.

6. Conclusions

The Pinyon Flat broadband array is an exceptional installation. Inverted amplitude statics coefficients are within theoretical design parameters of the seismometers and instrument orientations with respect to north are all, save one, within 2° of the average relative orientation. Because the amplitude statics coefficients correlate so well with instrument type, there is no obvious evidence for differential site effects causing amplitude differences among the sensors. Intuitively, this makes sense since the long-period teleseismic waves used for calibrating the array are 2 orders of magnitude larger than the array aperture.

Clear separation of instrument type using the proposed calibration method suggests that instrument manufacturers use equipment fabrication methods that are self-consistent and precise that yield relative performances better than advertised absolute performance. This, in turn, suggests that high-performance geodetic arrays should consist of a set of homogeneous instruments and not mixed instruments and data recording systems from different manufacturers. Additionally, differences between sensors and data acquisition systems can likely be quantified to a higher precision in the laboratory to produce higher resolution response information than is currently available. Having this high-resolution response information would simplify the analysis of geodetic array data since horizontal sensor orientation would be the only unknown parameter in characterizing stations of the array.

The ability to calibrate a geodetic seismic array to better than 0.5% in amplitude and 0.4° in orientation pushes the accuracy of computed spatial wave gradients a little beyond the bounds suggested by Langston (2007b) where a second-order finite difference gradient calculation requires that the station spacing be 1% of the maximum wavelength. Inclusion of multiply distributed stations, a third-order gradient calculation that allows inhomogeneous strain, and no explicit reference station in the gradient inversion offers a significant improvement over the second-order estimate.

In situ calibration of the Pinyon Flat array was useful as a data quality control method and resulted in improvements to computed wave spatial gradients. Comparison of array strains with strains from the B084 GTSM for a regional earthquake is encouraging and suggests that PBO borehole strainmeters, in conjunction with a single broadband sensor, can be used as a point array for determining wave field attributes such as azimuth and wave slowness.

Appendix A

Here are the derivatives of equations (1.32) used in the horizontal component inversion.

$$\frac{\partial f_j}{\partial \beta_1} = -a_j C_{11} \sin\delta_{1j} \tag{A1}$$

$$\frac{\partial f_j}{\partial a_j} = \mathrm{A}_{11} \cos\delta_{1j} - \beta_1 C_{11} \sin\delta_{1j} \tag{A2}$$

$$\frac{\partial f_j}{\partial b_j} = 0 \tag{A3}$$

$$\frac{\partial f_j}{\partial \delta_{1j}} = -a_j A_{11} \sin\delta_{1j} - a_j \beta_1 C_{11} \cos\delta_{1j} \tag{A4}$$

$$\frac{\partial g_j}{\partial \beta_1} = b_j B_{11} \cos\delta_{1j} \tag{A5}$$

$$\frac{\partial g_j}{\partial a_j} = 0 \tag{A6}$$

$$\frac{\partial g_j}{\partial b_j} = C_{11}\sin\delta_{1j} + \beta_1 B_{11}\cos\delta_{1j} \tag{A7}$$

$$\frac{\partial g_j}{\partial \delta_{1j}} = b_j C_{11}\cos\delta_{1j} - b_j\beta_1 B_{11}\sin\delta_{1j} \tag{A8}$$

$$\frac{\partial h_j}{\partial \beta_1} = b_j C_{11}\cos\delta_{1j} \tag{A9}$$

$$\frac{\partial h_j}{\partial a_j} = 0 \tag{A10}$$

$$\frac{\partial h_j}{\partial b_j} = A_{11}\sin\delta_{1j} + \beta_1 C_{11}\cos\delta_{1j} \tag{A11}$$

$$\frac{\partial h_j}{\partial \delta_{1j}} = b_j A_{11}\cos\delta_{1j} - b_j\beta_1 C_{11}\sin\delta_{1j} \tag{A12}$$

$$\frac{\partial k_j}{\partial \beta_1} = -a_j B_{11}\sin\delta_{1j} \tag{A13}$$

$$\frac{\partial k_j}{\partial a_j} = C_{11}\cos\delta_{1j} - \beta_1 B_{11}\sin\delta_{1j} \tag{A14}$$

$$\frac{\partial k_j}{\partial b_j} = 0 \tag{A15}$$

$$\frac{\partial k_j}{\partial \delta_{1j}} = -a_j C_{11}\sin\delta_{1j} - a_j\beta_1 B_{11}\cos\delta_{1j} \tag{A16}$$

Acknowledgments

This research was supported by National Science Foundation grant EAR 1460377 and is gratefully acknowledged. The author also thanks Frank Vernon for his help in tracking down the error in the array metadata, supplying an array history, and, of course, for installing such a high-quality array at Pinyon Flat. Data for the PY array (https://doi.org/10.7914/SN/PY), PFO station (https://doi.org/10.7914/SN/AZ), and B084 GTSM are openly available from the Incorporated Research Institutions in Seismology (IRIS) Data Management Center. The use of IRIS facilities is gratefully acknowledged and made this work possible. The author also thanks the two anonymous reviewers and Associate Editor Yehuda Ben-Zion for their useful comments that improved the manuscript.

References

Aderhold, K., Anderson, K. E., Reusch, A. M., Pfeifer, M. C., Aster, R. C., & Parker, T. (2015). Data quality of collocated portable broadband seismometers using direct burial and vault emplacement. *Bulletin of the Seismological Society of America*, *105*(5), 2420–2432. https://doi.org/10.1785/0120140352

Barker, L. M., & Langston, C. A. (2016). Small-scale Array experiments in seismic-wave gradiometry. *Seismological Research Letters*, *87*(5), 1091–1103. https://doi.org/10.1785/0220160040

Bronshtein, I. N., Semendyayev, K. A., Musiol, G., & Muehlig, H. (2004). *Handbook of mathematics* (4th ed.). Berlin, New York: Springer. https://doi.org/10.1007/978-3-662-05382-9

Davis, P., Ishii, M., & Masters, G. (2005). An assessment of the accuracy of GSN sensor response information. *Seismological Research Letters*, *76*(6), 678–683. https://doi.org/10.1785/gssrl.76.6.678

de Ridder, S. A. L., & Curtis, A. (2017). Seismic Gradiometry using ambient seismic noise in an anisotropic Earth. *Geophysical Journal International*. https://doi.org/10.1093/gji/ggx073

Donner, S., Lin, C.-J., Hadziioannou, C., Gebauer, A., Vernon, F., Agnew, D. C., et al. (2017). Comparing direct observation of strain, rotation, and displacement with array estimates at Piñon flat observatory, California. *Seismological Research Letters*, *88*(4), 1107–1116. https://doi.org/10.1785/0220160216

Ekstrom, G., & Busby, R. W. (2008). Measurements of seismometer orientation at USArray transportable array and backbone stations. *Seismological Research Letters*, *79*(4), 554–561. https://doi.org/10.1785/gssrl.79.4.554

Ekström, G., Dalton, C. A., & Nettles, M. (2006). Observations of time-dependent errors in long-period instrument gain at global seismic stations. *Seismological Research Letters*, *77*(1), 12–22. https://doi.org/10.1785/gssrl.77.1.12

Grant, E. (2010). Gladwin tensor strainmeter calibration using seismic data: Instrument calibration methods and wave gradiometry applications. (PhD thesis), University of Memphis, Memphis.

Hodgkinson, K., Langbein, J., Henderson, B., Mencin, D., & Borsa, A. (2013). Tidal calibration of plate boundary observatory borehole strainmeters. *Journal of Geophysical Research: Solid Earth*, *118*, 447–458. https://doi.org/10.1029/2012JB009651

Hutt, C. R., & Ringler, A. T. (2011). Some possible causes of and corrections for STS-1 response changes in the global seismographic network. *Seismological Research Letters*, *82*(4), 560–571. https://doi.org/10.1785/gssrl.82.4.560

Kromer, R. P. (2006a). Evaluation of the Kinemetrics/Quanterra Q330HR remote seismic system for IRIS/GSN (Progress Report). Retrieved from http://www.iris.edu/hq/files/programs/gsn/documents/IRIS_Progress_Report2_Q330HR.pdf

Kromer, R. P. (2006b). Evaluation of the Refraction Technology RT130HR remote seismic system for IRIS/GSN (Progress Report). Retrieved from http://www.iris.edu/hq/files/programs/gsn/documents/IRIS_Progress_Report2_RT130HR.pdf

Langston, C. A. (2007a). Spatial gradient analysis for linear seismic arrays. *Bulletin of the Seismological Society of America*, *97*(1B), 265–280. https://doi.org/10.1785/0120060100

Langston, C. A. (2007b). Wave Gradiometry in two dimensions. *Bulletin of the Seismological Society of America*, *97*(2), 401–416. https://doi.org/10.1785/0120060138

Langston, C. A., & Liang, C. (2008). Gradiometry for polarized seismic waves. *Journal of Geophysical Research*, *113*, B08305. https://doi.org/10.1029/2007JB005486

Liang, C., & Langston, C. A. (2009). Wave gradiometry for USArray: Rayleigh waves. *Journal of Geophysical Research*, *114*, B02308. https://doi.org/10.1029/2008JB005918

Liu, Y., & Holt, W. E. (2015). Wave gradiometry and its link with Helmholtz equation solutions applied to USArray in the eastern U.S. *Journal of Geophysical Research: Solid Earth*, *120*, 5717–5746. https://doi.org/10.1002/2015JB011982

Poppeliers, C., & Evans, E. V. (2015). The effects of measurement uncertainties in seismic-wave gradiometry. *Bulletin of the Seismological Society of America*, *105*(6), 3143–3155. https://doi.org/10.1785/0120150043

Ringler, A. T., Hutt, C. R., Persefield, K., & Gee, L. S. (2013). Seismic station installation orientation errors at ANSS and IRIS/USGS stations. *Seismological Research Letters*, *84*(6), 926–931. https://doi.org/10.1785/0220130072

Spudich, P., Steck, L. K., Hellweg, M., Fletcher, J. B., & Baker, L. M. (1995). Transient stresses at Parkfield, California, produced by the M7.4 Landers earthquake of June 28, 1992: Observations from the UPSAR dense seismograph array. *Journal of Geophysical Research*, *100*, 675–690. https://doi.org/10.1029/94JB02477

Tasič, I., & Runovc, F. (2013). Determination of a seismometer's generator constant, azimuth, and orthogonality in three-dimensional space using a reference seismometer. *Journal of Seismology*, *17*(2), 807–817. https://doi.org/10.1007/s10950-012-9355-y

Trimble (2017). Retrieved from http://trl.trimble.com/docushare/dsweb/Get/Document-582036/022543-536C_GeoXR_DS_0413_LR.pdf

VanDecar, J. C., & Crosson, R. S. (1990). Determination of teleseismic relative phase arrival times using multi-channel cross-correlation and least squares. *Bulletin of the Seismological Society of America*, *80*, 150–169.

Wielandt, E. (2002). Seismometry. In W. H. K. Lee, et al. (Eds.), *International handbook of earthquake and engineering seismology, Part A* (Chap. 18, pp. 283–304). London: Academic Press. https://doi.org/10.1016/S0074-6142(02)80221-2